Trapped water molecules are essential to structural dynamics and function of a ribozyme

Maria M. Rhodes*, Kamila Réblová†, Jiří Šponer†‡§, and Nils G. Walter*§

*Department of Chemistry, Single Molecule Analysis Group, University of Michigan, 930 North University Avenue, Ann Arbor, MI 48109-1055; †Institute of Biophysics, Academy of Sciences of the Czech Republic, Královopolská 135, 612 65 Brno, Czech Republic; and ‡Institute of Organic Chemistry and Biochemistry, Academy of Sciences of the Czech Republic, 166 10 Prague 6, Czech Republic

Edited by Jennifer A. Doudna, University of California, Berkeley, CA, and approved July 19, 2006 (received for review June 17, 2006)

Ribozymes are catalytically competent examples of highly structured noncoding RNAs, which are ubiquitous in the processing and regulation of genetic information. Combining explicit-solvent molecular dynamics simulation and single molecule fluorescence spectroscopy approaches, we find that a ribozyme from a subviral plant pathogen exhibits a coupled hydrogen bonding network that communicates dynamic structural rearrangements throughout the catalytic core in response to site-specific chemical modification. Trapped long-residency water molecules are critical for this network and only occasionally exchange with bulk solvent as they pass through a breathing interdomain base stack. These highly structured water molecules line up in a string that may potentially also be involved in specific base catalysis. Our observations suggest important, still underappreciated roles for specifically bound water molecules in the structural dynamics and function of noncoding RNAs.

coupled molecular motions | hairpin ribozyme | molecular dynamics | proton wire | specific base catalysis

Water is the universal solvent that supports all known forms of life. It is known to bind and stabilize the native structures of biopolymers such as RNA (1–10), but its precise role(s) in RNA function remain poorly understood. Highly structured noncoding (nc)RNAs, some endowed with catalytic functionality, have recently been recognized to outnumber protein-coding RNAs several-fold and to be of central importance in the processing and regulation of genetic information (11–13). Few techniques exist that can possibly provide insight into the intricate role(s) that water molecules play in the structure–function relationships of this important class of biopolymers. We here have applied a combination of explicit-solvent molecular dynamics (MD) and single-molecule FRET (smFRET) approaches to reveal support for two distinct roles for water molecules in the function of a particularly compact catalytic ncRNA, the hairpin ribozyme, derived from a subviral plant pathogen (12).

As is common for ncRNAs, the hairpin ribozyme relies on specific hydrogen bonding and base stacking to form an intricate tertiary structure with a solvent protected core (14). An interdomain $G+1$:C25 Watson–Crick base pair reinforced by a $G+1$:A38 stacking interaction, a 4-nt ribose zipper, and a specific hydrogen bonding pocket for an extruded U42 mediate docking of its domains A and B (Fig. 1*a*). smFRET studies have revealed the dynamic nature of these docking interactions (15–18), in which distal functional group modifications often significantly accelerate undocking. The latter observation led to the hypothesis that coupled molecular motions interconnect distal segments of the RNA (17). We here have confirmed this view by tracking the underlying hydrogen bonding network and finding that single water molecules trapped in the solvent protected catalytic core are integral components of this network.

Despite intense efforts, the catalytic mechanism of the hairpin ribozyme is still ill-understood. Functional groups of the RNA, rather than metal cofactors, have been proposed to catalyze site-specific backbone phosphodiester transfer (12, 14, 19, 20). Crystal structures (14, 19) have found the imino group of G8 within hydrogen bonding distance of the 2′-hydroxyl (2′-OH) of A-1, which needs to be deprotonated in the initial base catalysis step (12, 14). However, only non-physiologically high pH would deprotonate the G8 imino group to act as a general base; therefore, alternative proposals have been developed where G8 either acts via a tautomeric intermediate (21) or stabilizes the transition state by electrostatics (22) and/or hydrogen bonding (9, 19). Our MD simulations suggest that specific base catalysis by pK_a-shifted single water molecules trapped in the catalytic core must also be considered a plausible catalytic strategy for RNA.

Results

Supporting Information. For further details, see Figs. 4–17, Tables 1–5, and *Supporting Text*, which are published as supporting information on the PNAS web site.

Structural Dynamics from Explicit-Solvent Molecular Dynamics Simulations. We have performed altogether 12 (accumulative: ≈150 ns) explicit-solvent, charge-neutralized MD simulations (Table 1; with and without six crystallographically placed Mg^{2+} ions) on a truncated form of the 2.4-Å resolution precatalytic hairpin ribozyme crystal structure (Fig. 1*a*), using our well established protocols (5, 8, 23–25). We separately introduced two single-functional group modifications, 2′-deoxy-A38 (dA38) and 2′-deoxy-G11 (dG11), and two single-nucleotide mutations, $G+1$A and U42C, to closely mimic the variants used in our smFRET experiments that show the most significant acceleration of undocking (16, 17) (Fig. 1*a*). Fig. 4*b* illustrates the generally good agreement between the per-nucleotide rmsd over 10 ns of MD simulation and the B (“temperature”) factors of the two available crystal structures (7, 14), suggesting that our MD simulations realistically represent structural dynamics in the hairpin ribozyme.

Structural Communication Through a Long-Range Hydrogen Bonding Network Involving Water Molecules. Cross-correlation matrices of motions in different solute segments over an MD simulation provide insight into coupled (correlated or anticorrelated) motions and assess differences between mutant MD simulations (26). Our simulations show marked differences in cross-correlations that correspond well with our smFRET data (Figs. 1*b* and 4*c*). Most strikingly, the dA38 variant loses the WT correlation of U42 with domain A motions, indicating the loss of

Conflict of interest statement: No conflicts declared.

This paper was submitted directly (Track II) to the PNAS office.

Abbreviations: ncRNA, noncoding RNA; MD, molecular dynamics; smFRET, single-molecule FRET; dA38, 2′-deoxy-A38; dG11, 2′-deoxy-G11; ESP, electrostatic potential; IAA, in-line attack angle.

§To whom correspondence may be addressed. E-mail: nwalter@umich.edu or sponer@ncbr.chemi.muni.cz.

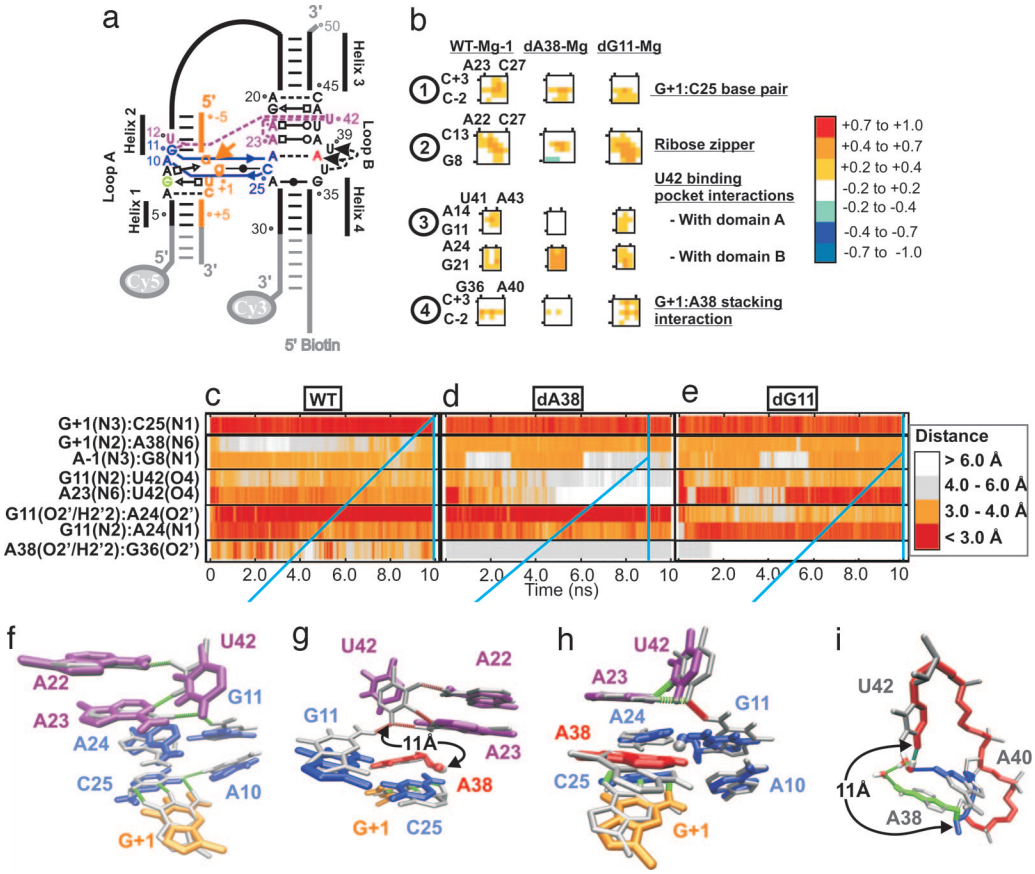

Fig. 1. MD simulations of the hairpin ribozyme. (*a*) Secondary and tertiary structure of the simulated docked WT hairpin ribozyme (orange, substrate) (14); gray segments were present in our smFRET experiments but omitted in MD. Solid horizontal lines represent Watson–Crick base pairs. Specific hydrogen bond interactions are annotated with circles (Watson–Crick), squares (Hoogsteen), and triangles (sugar edge), either filled (cis-interaction) or open (trans). Dashed lines, single hydrogen bonds; dashed bent arrows, backbone turns; orange arrow, cleavage site. (*b*) Specific cross-correlation analyses for the interdomain interactions by nucleotide of the first 10 ns of three representative MD simulations (WT-Mg-1, dA38-Mg, and dG11-Mg). The scale is shown at right. (*c–e*) Specific (hydrogen bonding) distance density plots over the first 10 ns of MD simulations WT-Mg-1 (*c*), dA38-Mg (*d*), and dG11-Mg (*e*); the color scale is shown at right. At defined times (cyan lines; WT-Mg-1, 9.9–10 ns; dA38-Mg, 9.0–9.1 ns; dG11-Mg, 9.9–10 ns), snapshots of key nucleotides averaged over each 100 ps were laid (in color) over the WT crystal structure (silver) for simulations WT-Mg-1 (*f*), dA38-Mg (*g*), and dG11-Mg (*h*), as indicated; crystal structure hydrogen bonds that are maintained until the end of the simulation are in green, and hydrogen bonds lost during the simulation are in red. (*i*) Three typical paths through covalent and hydrogen bonds (blue and green, respectively) or only covalent bonds (red), indicating that the shortest connection between the communicating A38(O2′) and U42(O4) is across a hydrogen bonding network involving water molecules trapped in the catalytic core.

the interdomain portion of the U42 binding pocket, whereas U42's correlated motions with domain B are strengthened; dA38 also loses correlated motions in the ribose zipper. This finding indicates severe impairment of docking interactions in dA38, in accord with the experimentally observed 65-fold accelerated undocking (17). The dG11 variant shows more subtle changes, including expanded correlated motions in the ribose zipper and $G+1$:A38 stack combined with weakened $G+1$:C25 correlations (Fig. 1*b*). This finding corresponds well with the moderately (≈12-fold) accelerated undocking (16). Finally, the $G+1$A and U42C mutants show substantially and moderately diminished correlated motions, respectively (Figs. 8*a* and 9*a*), paralleling their experimentally observed undocking accelerations (16, 17).

Upon closer inspection, all four WT simulations (total: 60 ns, Table 1) maintain all interdomain hydrogen bonds in the catalytic core (Fig. 1*c*) and stay close to the starting structure (Figs. 1*f*, 7, 10, and 11). The $G+1$:A38 stack [tracked as $G+1$(N2):A38(N6)] in simulation WT-Mg-1 opens to >6 Å after 400 ps but closes again by 10 ns, indicating "breathing" dynamics (Fig. 1*c*). The other core stacking interaction, between A-1 and G8 [tracked as A-1(N3):G8(N1), Fig. 1*c*], remains intact. By contrast, the two dA38 simulations lose within a few ns key U42 hydrogen bonds (Figs. 1*d* and 12*b*) as the U42 Watson–Crick face rotates 180° away from domain A (Figs. 1*g* and 12*c*), resulting in the lost U42 cross-correlations of Fig. 1*b*. Remarkably, the lost U42 hydrogen bonds are far away (≈11 Å) from the 2′-deoxy-A38 modification. The shortest connection between 2′-deoxy-A38 and U42(O4) is through 11 covalent and four hydrogen bonds, involving several buried water molecules in the catalytic core (Fig. 1*i*). These observations suggest that a long-range network of directional noncovalent and covalent bonds exists that involves critically located water molecules and effects correlated molecular motions and structural communication throughout the catalytic core. This finding contrasts the dynamics of globular proteins, which are typically dominated by non-directional hydrophobic interactions (27).

The notion of a long-range hydrogen bonding network is further supported by the dG11 modification, which eliminates the G11(O2′):A24(O2′) hydrogen bond and partially disrupts the ribose zipper. In our two MD simulations of this variant, the local structure adjusts to reinforce the G11(N2):A24(N1) hydrogen bond instead (Figs. 1*e* and 13). This compensatory structural rearrangement explains the expanded cross-correlation of the ribose zipper in Fig. 1*b*. However, this finding

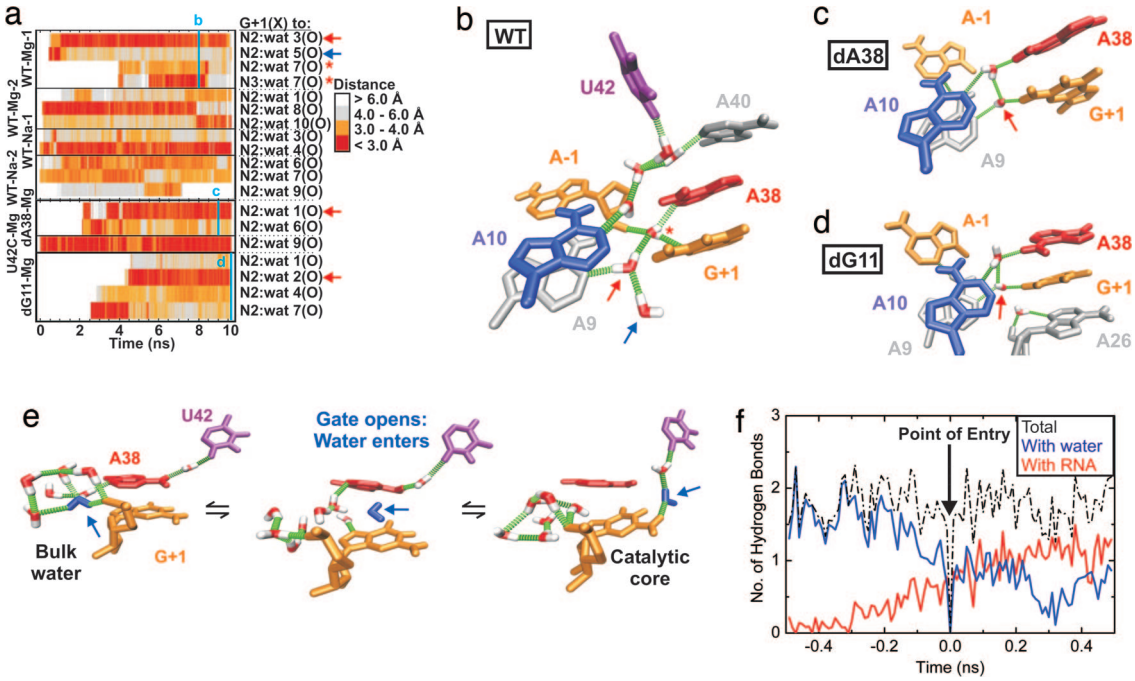

Fig. 2. Select water molecules enter the catalytic core cavity. (*a*) Distances of specific water molecules to functional groups on $G+1$ for all WT simulations and simulations of several ribozyme variants, as indicated. Vertical cyan lines indicate times from which snapshots for *b*–*d* were taken. The asterisk and arrow mark the same water molecules as in *b* and Fig. 3 *a* and *b*. (*b*) Averaged snapshot (7.9–8.0 ns) of simulation WT-Mg-1, with the hydrogen bonding network of the seven intracavity water molecules indicated in green. The asterisk and arrow mark the analogous water molecules as in Fig. 3 *a* and *b*. (*c*) Averaged snapshot (9.0–9.1 ns) of simulation dA38-Mg. (*d*) Averaged snapshot (9.9–10.0 ns) of simulation dG11-Mg. (*e*) A water molecule from bulk solvent enters the catalytic core as the $G+1$:A38 stack opens in a gate-like fashion. (*f*) Number of hydrogen bonds observed for a water molecule before and after it enters the catalytic core, averaged over all 14 water molecules that enter through the $G+1$:A38 in simulations WT-Mg-1 and WT-Mg-2.

weakens the $G+1$:C25 base pair, as indicated by a diminished cross-correlation and a decrease in occupancy of a strong (<3 Å) $G+1$(N3):C25(N1) hydrogen bond from 74.6% in the WT to 50.5% in one of the dG11 simulations (Figs. 1 *c* and *e*). This weakening, in turn, allows $G+1$ to become more cross-correlated with A38 (Fig. 1*b*). Again, a single functional group modification leads to correlated structural rearrangements throughout the catalytic core, most plausibly mediated by the hydrogen bonding network described above. Similarly, the $G+1$A mutation disrupts the central interdomain $G+1$:C25 base pair (Fig. 1*a*). In both $G+1$A simulations, all interdomain contacts are lost within 2 ns as $A+1$ turns its Watson–Crick face away from C25 (although some compensatory interactions form, Figs. 8 and 14). Finally, the U42C mutant, expected to disrupt three hydrogen bonds in the U42 binding pocket, shows only moderate structural changes. In both simulations of this variant, C42 retains a hydrogen bond with A22(N6), whereas the occupancy of its hydrogen bond with A23 is reduced and the hydrogen bond with G11(N2) is entirely lost (Figs. 9 and 15).

Quantitative Agreement Between MD Simulations and smFRET Experiments. To quantify the structural rearrangements upon local modification, we inventoried the direct RNA-RNA interdomain hydrogen bonds after 10-ns simulation (*Supporting Text*). The WT simulations lose an average of only 0.05 interdomain hydrogen bonds relative to the equilibrated crystal structure, whereas the ribozyme variants lose 1.01–4.03 hydrogen bonds. Significantly, we find a linear relationship (correlation coefficient $r = 0.98$) between this loss of hydrogen bonds and the loss of docking free energy relative to the WT ($\Delta\Delta G_{dock}$), derived from our smFRET experiments (Fig. 5). The linear slope predicts a free energy of 2.4 ± 0.3 kcal/mol per lost interdomain hydrogen bond, in reasonable agreement with experimental measurements of 0.5 to 2.2 kcal/(mol hydrogen bond) in RNA (28, 29). These observations imply that 10-ns MD simulations starting from the docked crystal structure provide plausible models for the structures probed in docking experiments.

Long-Residency Water Molecules Occupy the Interdomain Cavity. The catalytic core of the WT crystal structure contains a 350-Å^3 interdomain cavity (see *Supporting Text*). Our simulations were initiated from the crystal structure without water molecules in the cavity (14). Early in our WT MD simulations, five to seven water molecules enter the cavity (Figs. 2 *a* and *b* and 16*a*), which has a fluctuating volume of 390 ± 210 Å^3. The water molecules arrange as an interconnected string with up to 16 total hydrogen bonds with each other and RNA functional groups (Fig. 2*b*), thereby forming a key component of the coupled hydrogen bonding network in the catalytic core (Fig. 1*i*). The site-specific modifications reduce the interdomain cavity size and the number of intracavity water molecules. For example, dA38 harbors two water molecules in a cavity of 120 ± 70 Å^3 (Fig. 2*c*), whereas dG11 retains three in a 180 ± 110 Å^3 cavity (Fig. 2*d*). Two hydration sites are occupied in all WT and variant simulations in Mg^{2+} and establish water bridges connecting $G+1$(N2) and A38(N6) with A9(N1) and A10(N1), respectively (Figs. 2*b* and 16). Additional locations are less frequently occupied in other simulations (Figs. 2 and 16). Hydrated sites stay occupied by the same trapped water molecule for 0.5–8.5 ns [as opposed to waters bound to the outside of RNA, which typically localize for only 0.05–0.5 ns (5, 24)], with only occasional interchange of intracavity waters (Fig. 2*a*) and total intracavity residence times of 4.1–29.4 ns. Notably, the locations of long-residency water molecules observed here for the WT are independently confirmed by electron densities from recent high-resolution x-ray diffraction studies (7) (Fig. 17).

Biochemical (30) and crystallographic experiments (7, 14) suggest that the catalytic core of the hairpin ribozyme is solvent-protected. Fourteen of the 16 water molecules that enter the catalytic core during our two Mg^{2+}-containing WT simulations exploit the stochastically breathing $G+1$:A38 stacking interaction as an entry gate that opens just wide enough to let a single water molecule pass; this and the limited cavity size appear to discriminate against larger water clusters (Fig. 2*e*). While passing between the hydrophobic, planar $G+1$ and A38 purine rings, single water molecules temporarily enter a state devoid of any hydrogen bonds (Fig. 2 *e* and *f*), analogous to the vapor-like state water is proposed to adopt during the hydrophobic collapse of a folding protein (31). We also observe six water molecules exiting the core by the same route and mechanism (Fig. 17), suggesting that the intracavity water slowly exchanges with bulk solvent.

The Catalytic Core Is Protected from Cations. Despite the fact that the catalytic core is characterized by a highly negative electrostatic surface potential (ESP; the minimum is −51 kT/e), not a single metal cation enters the catalytic core cavity in any of our MD simulations (except for the $G+1$A mutant simulations, where the core opens to solvent; Table 1). A control 30-ns WT simulation with a Na^+ cation initially placed within the cavity found that the cation moved toward the $G+1$:A38 gate but did not exit the cavity. Thus, we cannot rule out the possibility that a partly desolvated metal ion may occasionally get caught in the cavity, but an exchange of ions between core and bulk is likely not a frequent event (see *Supporting Text*). The protected catalytic core of the hairpin ribozyme thus strikingly contrasts with the rather open catalytic pocket of the hepatitis delta virus (HDV) ribozyme, which also has a highly negative ESP (minimum approximately −63 kT/e) and is occupied by either one divalent or two monovalent cations (10). Whereas the HDV ribozyme attracts these catalytic cations for potential participation in reaction chemistry (10), the hairpin ribozyme blocks cation access, exposing the trapped long-residency water molecules and proximal bases to the uncompensated negative ESP.

Trapped Intracavity Water Molecules Hydrogen Bond to the Catalytically Involved 2′-Hydroxyl Nucleophile. In our MD simulations, water molecules reside as an interconnected string within the catalytic core for many nanoseconds (Fig. 2). A hydrogen bond forms between a central one of these intracavity water molecules and the 2′-OH of A-1 (asterisks in Figs. 2*b* and 3) that acts as a nucleophile in the catalyzed backbone cleavage reaction. The water molecule is trapped near a highly negative ESP in the metal-cation-free core of the hairpin ribozyme (Fig. 3*b*). In all of our WT simulations, conformational relaxation of the A-1 sugar pucker from 2′-endo to the thermodynamically more stable 2′-exo conformation coincides with hydrogen bond formation (Fig. 3*c* and supporting information). This conformational change may be related to the fact that the catalysis-blocking methyl group, which caps the 2′-oxygen in the crystal structure, is removed in our A-1(2′-OH) carrying simulations. The same conformational relaxation has recently been observed in crystallographic studies that introduced the 2′-OH into A-1 (7). Notably, several other 2′-endo sugar puckers in the RNA do not change to the 2′-exo conformation during our simulations, whereas others repeatedly interconvert between both, suggesting that the directional conformational change observed for the A-1 ribose in all WT simulations is significant (supporting information). Upon interconversion, A-1(O2′) switches from accepting a hydrogen bond from G8(N1) in the crystal structure to accepting it from A9(N6) or, in some simulations, alternately A9(N6) and A10(N6) (Fig. 3*a*). These rearrangements initially decrease the nucleophilic in-line attack angle (IAA) for phosphodiester transfer [A-1(2′O)-$G+1$(P)-$G+1$(5′O)], which is thought to be optimal at 180° and observed to be between 136° and 158° in the crystal structures (7, 14, 19) (Fig. 3*b*). Although the A-1 sugar pucker never reverses to the unfavorable 2′-endo conformation, the IAA returns from ≈70° to an average of 115 ± 12° in three of our four WT simulations (Fig. 3*c*). Notably, this IAA is fully compatible with the hydrogen bond of 2′-OH to the central intracavity water molecule.

Discussion

We find here that the catalytic core of the hairpin ribozyme, a highly structured ncRNA, is characterized by a coupled hydrogen bonding network involving several long-residency water molecules. This network is the basis for correlated motions amplifying local chemical modifications into structural rearrangements throughout the catalytic core. Single water molecules briefly enter a state devoid of hydrogen bonds as they stochastically exchange between catalytic core and bulk solvent through a breathing purine stack and condense into a string of water molecules, which resembles the classic "proton wire" observed in protein enzymes (32). Such a wire is thought particularly suitable to conduct protons, because the initial proton transfer can occur at neutral pH in under 150 fs (33) and is followed by Grotthuss-type proton transfer to other water molecules within 30 fs (34, 35). By accepting a hydrogen bond from the 2′-OH of A-1, a central intracavity water molecule is in a perfect position to abstract and rapidly shuttle away the proton that triggers catalysis. This water molecule is trapped in a highly negatively charged pocket in the metal-cation-free core of the hairpin ribozyme (Fig. 3*b*), where its pK_a could potentially be shifted to bring it closer to the pK_a of the 2′-OH (≈13) than any functional group nearby. A recent MD simulation indicates that a hydrogen bond between A-1(O2′) and an intracavity water molecule is also formed in a transition state mimic of the hairpin ribozyme (9). Water molecules trapped in the catalytic core must therefore be considered strong potential candidates for specific base catalysis. Such a mechanism would identify the base responsible for initiating catalysis and be complementary to models asserting an important role for transition state stabilization by G8 through electrostatics (22) and/or hydrogen bonding (19). It would also explain why the hairpin ribozyme, when frozen at ≥−10°C, retains residual specific activity even in the absence of the substrate-binding strand containing G8 (36) and why inosine, which lacks only the exocyclic amino group of guanine, strongly impairs hairpin ribozyme activity when substituted into the +1 position (37). Inosine still fulfills the essential role of Watson–Crick base pairing with C25 (Fig. 1*a*) but no longer supplies the structural $G+1$(N2) anchor for the proton wire (Fig. 2).

In summary, our studies support the notion that site-specifically bound water molecules endow certain highly structured ncRNAs with a diversified structural and catalytic repertoire. More specifically, the hairpin ribozyme is an example of an ncRNA that tightly folds around an interdomain, solvent-protected cavity, trapping water molecules as integral components of the RNA fold. Solvent-protected RNA domains are frequently observed in highly structured ncRNAs, suggesting that water capture for integration into RNA structure and function may be a common principle. Our results suggest an important role for trapped water molecules in the structural communication afforded by coupled molecular motions throughout the folded core of an ncRNA. This role is facilitated by the many functional groups in RNA which can form strong hydrogen bonds with water; this may represent a fundamental distinction from proteins, where hydrophobic van der Waals interactions often completely exclude water molecules from a folded core (27, 31). Our work helps establish explicit-solvent MD simulations as a powerful tool to track the hydrogen bonding networks underlying long-range structural communication throughout ncRNAs. This finding paves the road to a deeper understanding of the underappreciated roles of water in the folding and function of RNA (3, 6). Future progress will likely

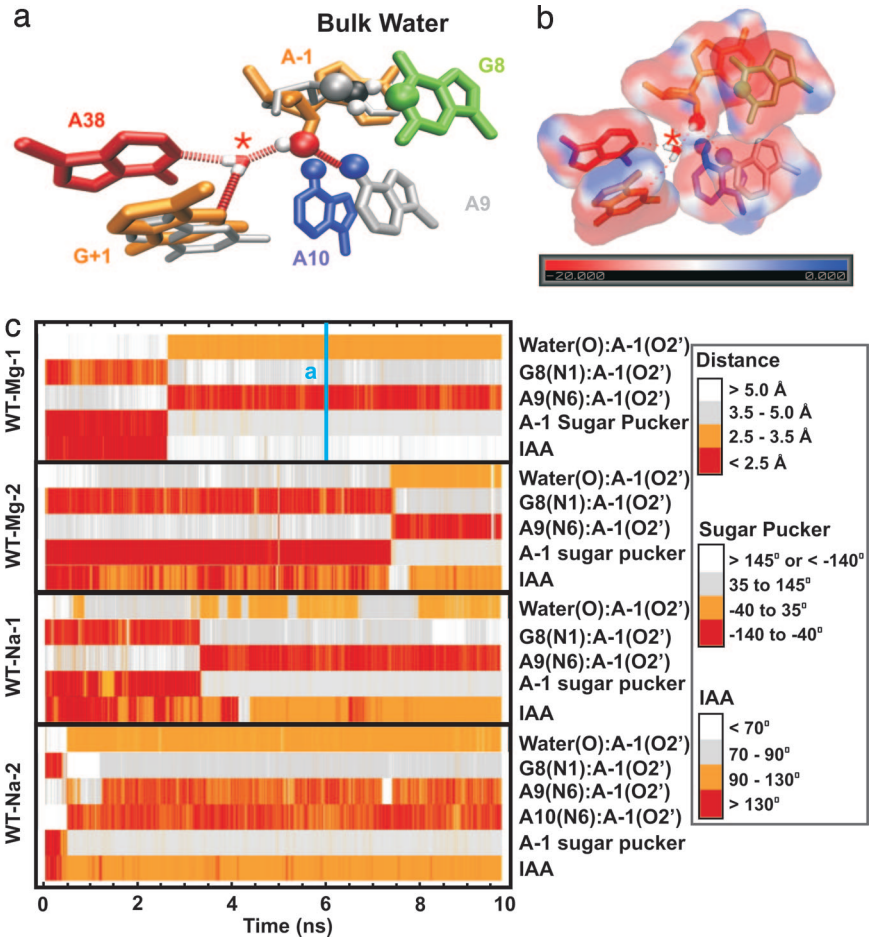

Fig. 3. Possible catalytic role of intracavity water. (*a*) Upon removal of A-1(O2′)'s catalysis-blocking methyl cap (black and white spheres), the 2′-OH of A-1 (red and white spheres) moves from bulk solvent into the catalytic core, establishing a hydrogen bond with the asterisked water molecule in the intradomain cavity (same water that is shown with an asterisk in Figs. 2 and 3*b*). Colored bases are from simulation WT-Mg-1 (averaged from 5.9–6.0 ns; cyan line in *c*); thinned gray bases, from the crystal structure (14). The green sphere marks G8(N1), A-1(O2′)'s hydrogen bonding partner in the crystal structure; blue spheres indicate A9(N6) and A10(N6), A-1(O2′)'s primary partners in the MD simulations. (*b*) Electrostatic potential map calculated for the complete structure and represented as van der Waals surface over the catalytic core residues shown in *a* and color-coded from −20 to 0 kT/e. The electrostatic potential minimum of −51 kT/e is near the asterisked water. (*c*) Density plots for the WT simulations, as indicated, demonstrating that movement of A-1(O2′) to hydrogen bond with an intracavity water and A9(N6)/A10(N6) coincides with changes in the A-1 sugar pucker and IAA. The water distance is measured to the closest intracavity water, which occasionally switches during simulations (compare with Fig. 2*a*).

be aided by the application of distributed computing to extend the MD simulation time scale (6), as well as the parallel use of experimental techniques such as NMR spectroscopy to detect cross-relaxation between water and specific RNA nuclei (4) and Fourier transform infrared (FTIR) spectroscopy to track the hydrogen bonding and protonation states of intracavity water clusters (35).

Methods

MD: Initial Structures and Cation Placement. Twelve MD simulations were started from the 2.4-Å resolution precatalytic hairpin ribozyme structure (Protein Data Bank ID code 1HP6) (14). Domains C and D were deleted in the conversion to the minimal, catalytically fully active two-way junction form; helix 1 and helix 4 were truncated to further reduce the computational cost with minimal effect on structural stability during the simulation. Addition of hydrogen atoms to the crystal structure, base modifications, and mutations were performed via InsightII. A catalysis-blocking methyl group attached to the 2′-oxygen of A-1 in the crystal structure was replaced by the native 2′-OH in all simulations. The Leap module from the AMBER suite was used to replace six Ca^{2+} ions found in the crystal structure with Mg^{2+} ions and to place 41 neutralizing Na^{+} ions initially at points of favorable electrostatic potential close to the RNA to achieve charge neutrality for the dual-ion simulations (effective concentrations: 30 mM Mg^{2+} and 200 mM Na^{+}) (38); in the Na^{+}-only simulations, 53 sodium ions were placed with the LeaP module (effective concentration: 260 mM Na^{+}). Our modeling of Na^{+}-only conditions is validated by the fact that the hairpin ribozyme is highly active in monovalent ions alone (39) (Fig. 6).

MD Equilibration and Simulation. All MD simulations were carried out by using the AMBER 6.0 program package (40) with the parm99 Cornell *et al.* force field (41–43). The initial structures were solvated in a rectangular periodic box of TIP3P waters extending ≥10 Å from the RNA. The Sander module of AMBER 6.0 was used for the equilibration and production simulations based on standard protocols (5, 8, 10, 23–25). The particle mesh Ewald method (44) was applied with a heuristic pair list update, using a 2.0-Å non-bonded pair list buffer and a 9.0-Å cutoff. A charge grid spacing of close to 1 Å and a cubic interpolation scheme were used. The production runs were carried out at 300 K with constant-pressure boundary conditions

using the Berendsen temperature coupling algorithm (45) with a time constant of 1.0 ps. SHAKE (46) was applied with a tolerance of 10^{-8} to constrain bonds involving hydrogens.

MD Analysis. Production trajectories were analyzed by using the carnal and ptraj modules of the AMBER 6.0 and AMBER-8 packages; perl scripts were used to identify and track important solvent molecules (*Supporting Text*). The ptraj module of AMBER 6.0 was used to obtain rmsd values, distances, angles, and pseudorotation angles of the riboses; that of AMBER 8 was used to obtain cross-correlation matrices; rmsd values were calculated by nucleotide over the entire simulation and then time-averaged. Cross-correlation matrices were calculated by nucleotide over the initial 10 ns of each simulation. Density figures were made from the ptraj output by using Mathematica 5.

We thank Hashim Al-Hashimi, Gordon Crippen, Joseph Wedekind, Daniel Herschlag, Vijay Pande, Ken Hampel, and members of the Walter group for the critical reading of the manuscript. This work was supported by National Institutes of Health Grant GM62357 including supplement S2 for acquisition of a computer cluster (to N.G.W.); a predoctoral fellowship from the National Science Foundation (to M.M.R.); Wellcome Trust Grant GR067507; Grant Agency Grants GA203/05/0009 and GA203/05/0388; Internal Grant Agency Grant 1QS500040581; and Ministry of Education, Youth, and Sports Grants LC06030, LC512, MSM0021622413, AVOZ50040507, and AVOZ40550506 (to J.Š. and K.R.).

1. Westhof, E., Dumas, P. & Moras, D. (1988) *Biochimie* **70,** 145–165.
2. Beveridge, D. L. & McConnell, K. J. (2000) *Curr. Opin. Struct. Biol.* **10,** 182–196.
3. Auffinger, P. & Westhof, E. (2000) *Biopolymers* **56,** 266–274.
4. Newby, M. I. & Greenbaum, N. L. (2002) *Proc. Natl. Acad. Sci. USA* **99,** 12697–12702.
5. Reblova, K., Spackova, N., Koca, J., Leontis, N. B. & Sponer, J. (2004) *Biophys. J.* **87,** 3397–3412.
6. Sorin, E. J., Rhee, Y. M. & Pande, V. S. (2005) *Biophys. J.* **88,** 2516–2524.
7. Salter, J., Krucinska, J., Alam, S., Grum-Tokars, V. & Wedekind, J. E. (2006) *Biochemistry* **45,** 686–700.
8. Spackova N. & Sponer, J. (2006) *Nucleic Acids Res.* **34,** 697–708.
9. Park, H. & Lee, S. (2006) *J. Chem. Theory Comp.* **2,** 858–862.
10. Krasovska, M. V., Sefcikova, J., Reblova, K., Schneider, B., Walter, N. G. & Sponer, J. (2006) *Biophys. J.* **91,** 626–638.
11. Carninci, P., Kasukawa, T., Katayama, S., Gough, J., Frith, M. C., Maeda, N., Oyama, R., Ravasi, T., Lenhard, B., Wells, C., *et al.* (2005) *Science* **309,** 1559–1563.
12. Doudna, J. A. & Lorsch, J. R. (2005) *Nat. Struct. Mol. Biol.* **12,** 395–402.
13. Zamore, P. D. & Haley, B. (2005) *Science* **309,** 1519–1524.
14. Rupert, P. B. & Ferre-D'Amare, A. R. (2001) *Nature* **410,** 780–786.
15. Zhuang, X., Kim, H., Pereira, M. J., Babcock, H. P., Walter, N. G. & Chu, S. (2002) *Science* **296,** 1473–1476.
16. Bokinsky, G., Rueda, D., Misra, V. K., Rhodes, M. M., Gordus, A., Babcock, H. P., Walter, N. G. & Zhuang, X. (2003) *Proc. Natl. Acad. Sci. USA* **100,** 9302–9307.
17. Rueda, D., Bokinsky, G., Rhodes, M. M., Rust, M. J., Zhuang, X. & Walter, N. G. (2004) *Proc. Natl. Acad. Sci. USA* **101,** 10066–10071.
18. Nahas, M. K., Wilson, T. J., Hohng, S., Jarvie, K., Lilley, D. M. & Ha, T. (2004) *Nat. Struct. Mol. Biol.* **11,** 1107–1113.
19. Rupert, P. B., Massey, A. P., Sigurdsson, S. T. & Ferre-D'Amare, A. R. (2002) *Science* **298,** 1421–1424.
20. Wilson, T. J., Ouellet, J., Zhao, Z. Y., Harusawa, S., Araki, L., Kurihara, T. & Lilley, D. M. (2006) *RNA* **12,** 980–987.
21. Pinard, R., Hampel, K. J., Heckman, J. E., Lambert, D., Chan, P. A., Major, F. & Burke, J. M. (2001) *EMBO J.* **20,** 6434–6442.
22. Kuzmin, Y. I., Da Costa, C. P. & Fedor, M. J. (2004) *J. Mol. Biol.* **340,** 233–251.
23. Reblova, K., Spackova, N., Sponer, J. E., Koca, J. & Sponer, J. (2003) *Nucleic Acids Res.* **31,** 6942–6952.
24. Reblova, K., Spackova, N., Stefl, R., Csaszar, K., Koca, J., Leontis, N. B. & Sponer, J. (2003) *Biophys. J.* **84,** 3564–3582.
25. Krasovska, M. V., Sefcikova, J., Spackova, N., Sponer, J. & Walter, N. G. (2005) *J. Mol. Biol.* **351,** 731–748.
26. Ichiye, T. & Karplus, M. (1991) *Proteins* **11,** 205–217.
27. Benkovic, S. J. & Hammes-Schiffer, S. (2003) *Science* **301,** 1196–1202.
28. Turner, D. H., Sugimoto, N., Kierzek, R. & Dreiker, S. D. (1987) *J. Am. Chem. Soc.* **109,** 3783–3785.
29. Silverman, S. K. & Cech, T. R. (1999) *Biochemistry* **38,** 8691–8702.
30. Hampel, K., Walter, N. G. & Burke, J. M. (1998) *Biochemistry* **37,** 14672–14682.
31. Liu, P., Huang, X., Zhou, R. & Berne, B. J. (2005) *Nature* **437,** 159–162.
32. Frank, R. A., Titman, C. M., Pratap, J. V., Luisi, B. F. & Perham, R. N. (2004) *Science* **306,** 872–876.
33. Mohammed, O. F., Pines, D., Dreyer, J., Pines, E. & Nibbering, E. T. (2005) *Science* **310,** 83–86.
34. Geissler, P. L., Dellago, C., Chandler, D., Hutter, J. & Parrinello, M. (2001) *Science* **291,** 2121–2124.
35. Garczarek, F. & Gerwert, K. (2006) *Nature* **439,** 109–112.
36. Vlassov, A. V., Kazakov, S. A., Johnston, B. H. & Landweber, L. F. (2005) *J. Mol. Evol.* **61,** 264–273.
37. Chowrira, B. M., Berzal-Herranz, A. & Burke, J. M. (1991) *Nature* **354,** 320–322.
38. Aqvist, J. (1990) *J. Phys. Chem.* **94,** 8021–8024.
39. Murray, J. B., Seyhan, A. A., Walter, N. G., Burke, J. M. & Scott, W. G. (1998) *Chem. Biol.* **5,** 587–595.
40. Case, D. A., Pearlman, D. A., Caldwell, J. W., Cheatham, T. E., III, Wang, J., Ross, W. S., Simmerling, C. L., Darden, T. A., Merz, K. M., Stanton, R. V., *et al.* (2002) AMBER (Univ. of California, San Francisco), Version 7.
41. Cornell, W. D., Cieplak, P., Bayly, C. I., Gould, I. R., Merz, K. M., Ferguson, D. M., Spellmeyer, D. C., Fox, T., Caldwell, J. W. & Kollman, P. A. (1995) *J. Am. Chem. Soc.* **117,** 5179–5197.
42. Cheatham, T. E., Cieplak, P. & Kollman, P. A. (1999) *J. Biomol. Struct. Dyn.* **16,** 845–862.
43. Wang, J. M., Cieplak, P. & Kollman, P. A. (2000) *J. Comp. Chem.* **21,** 1049–1074.
44. Essmann, U., Perera, L., Berkowitz, M. L., Darden, T., Lee, H. & Pedersen, L. G. (1995) *J. Chem. Phys.* **103,** 8577–8593.
45. Berendsen, H. J. C., Postma, J. P. M., Vangunsteren, W. F., Dinola, A. & Haak, J. R. (1984) *J. Chem. Phys.* **81,** 3684–3690.
46. Ryckaert, J. P., Ciccotti, G. & Berendsen, H. J. C. (1977) *J. Comp. Chem.* **23,** 327–341.